

# Simulating turbulent mixing caused by local instability of internal gravity waves

Yohei Onuki<sup>1†</sup>, Sylvain Joubaud<sup>2,3</sup> and Thierry Dauxois<sup>2</sup>

<sup>1</sup>Research Institute for Applied Mechanics, Kyushu University, 6-1 Kasuga-koen, Kasuga, Fukuoka, Japan

<sup>2</sup>Université de Lyon, ENS de Lyon, Université Claude Bernard, CNRS, Laboratoire de Physique, F-69342 Lyon, France

<sup>3</sup>Institut Universitaire de France, France

(Received xx; revised xx; accepted xx)

With the aim of assessing internal wave-driven mixing in the ocean, we develop a new technique for direct numerical simulations of stratified turbulence. Since the spatial scale of oceanic internal gravity waves is typically much larger than that of turbulence, fully incorporating both in a model would require a high computational cost, and is therefore out of our scope. Alternatively, we cut out a small domain periodically distorted by an unresolved large-scale internal wave and locally simulate the energy cascade to the smallest scales. In this model, even though the Froude number of the outer wave,  $Fr$ , is small such that density overturn or shear instability does not occur, a striped pattern of disturbance is exponentially amplified through a parametric subharmonic instability. When the disturbance amplitude reaches the overturning threshold, secondary instabilities arise and produce much smaller-scale fluctuations. Passing through these two stages, wave energy is transferred into turbulence energy and will be eventually dissipated. Different from the conventional scenarios of vertical shear-induced instabilities, a large part of turbulent potential energy is supplied from the outer wave and directly used for mixing. The mixing coefficient  $\Gamma = \epsilon_P/\epsilon$ , where  $\epsilon$  is the dissipation rate of turbulent kinetic energy and  $\epsilon_P$  is that of available potential energy, is always greater than 0.5 and tends to increase with  $Fr$ . This result challenges the recent scaling arguments on mixing efficiency in a stratified fluid.

## 1. Introduction

Diapycnal mixing in the mid-depth and deep ocean is a major contributor to the global overturning circulation that transports water mass, heat, and various biochemical substances (Munk & Wunsch 1998). Therefore, quantifying and parameterizing the small-scale turbulent mixing that cannot be resolved in ocean circulation models are crucial to our ability of predicting changes in the Earth's environment (MacKinnon *et al.* 2017).

The difficulty in understanding interior ocean mixing comes from the multi-scale nature of the system. The smallest length scale of the fluid motion that enhances heat conduction or salinity diffusion is normally  $O(1\text{cm})$  or much smaller (Thorpe 2005). Energy of this turbulent motion is mainly supplied from internal gravity waves, whose spatial scale is the order of tens or hundreds of meters. To fully assess the mixing in the ocean using a three-dimensional direct numerical simulation (DNS) model, accordingly, would need to incorporate larger than  $O(10^{12})$  grid points, which is an extremely challenging task even with the latest parallel computing systems.

† Email address for correspondence: onuki@riam.kyushu-u.ac.jp

Since the ordinary DNS cannot resolve both the typical scales of waves and turbulence, many studies simplify the problem. A widely considered situation is the mixing occurring in a vertically sheared horizontal flow due to Kelvin-Helmholtz or Holmboe instabilities (see, e.g., Smyth *et al.* 2001; Salehipour *et al.* 2016; Dauxois *et al.* 2020). In this case, the energy of turbulence is supplied from the kinetic energy of a background horizontal flow and will be redistributed to viscous dissipation and vertical buoyancy flux. In a stationary state, the vertical buoyancy flux coincides with the conversion rate from the available potential energy to the background potential energy. Since Osborn (1980), this energy balance has been regarded as representative in the ocean and a great attention has been directed to the ratio between the turbulence energy loss and the background potential energy gain, or the so-called mixing efficiency (Gregg *et al.* 2018). However, how well this simple model reflects the actual ocean conditions is still uncertain.

Generally speaking, internal wave energy is divided into the kinetic energy and the available potential energy. If rotation is excluded, these two are evenly partitioned. As was shown in laboratory experiments of Rayleigh-Taylor instability, when mixing is caused by the release of available potential energy through convection, the mixing efficiency becomes several factors higher than that in the cases of shear instability (Davies Wykes & Dalziel 2014). Accordingly, to fully understand the mixing caused by internal waves, it is vital to extend the discussion from classical shear instability to a wider variety of scenarios for turbulence generation.

The main purpose of the present study is to assess the efficiency of wave-driven mixing by using a new technique for simulating stratified turbulence. The model configuration is in part similar to Fritts *et al.* (2009). They examined a breaking internal gravity wave by resolving both the scales of waves and turbulence. In this study, on the other hand, with the aim of increasing the Reynolds number while reducing the computational cost, we do not resolve the largest wave component. Instead, we cut out a small domain periodically distorted by an unresolved outer wave, and simulate the excitation and dissipation of turbulence within it. In this model, the wave field is idealised as a spatially constant velocity shear, such that the turbulence enhanced in it is statistically homogeneous. Hence, we can assume periodic boundary conditions in all directions and employ the Fourier spectral discretisation, enabling precise representation of an energy cascade to the smallest dissipation scale.

As for homogeneous turbulence of stratified shear flow, there have been numerous studies using DNS (Portwood 2019, and references therein). They utilised a generic technique originally invented by Rogallo (1981) that we basically follow. However, the present study differs from the existing ones in two points:

1. In our model, the background shear varies periodically associated with the oscillation of the outer wave. As we shall see, this periodic variation causes parametric excitation of disturbances. Consequently, the turbulence energy is more easily amplified than in the conventional cases of stationary shear flow.
2. Since the buoyancy gradient is also changed by the outer wave, a fluid parcel crossing this gradient at some instant gains the available potential energy, which subsequently drives turbulent motion. This contrasts with the classical view of shear-driven mixing in a horizontal flow that is associated only with the shear production of kinetic energy.

In general, properties of stratified turbulence, including the mixing efficiency, are determined by the competing effects of buoyancy, inertia, viscosity and diffusion. Therefore, a thorough analysis requires to check the dependency of the experimental results on at least three dimensionless parameters. Among these, motivated by the suggestion of Maffioli *et al.* (2016) that competition between inertia and buoyancy is primarily important in

high-Reynolds number regimes, we vary here the Froude number of the outer wave that controls the energy level of turbulence while fixing the other parameters.

The paper is organised as follows. The model and the calculation methods are described in §2. We present the simulation results in §3 and discuss the mixing efficiency from an energetic viewpoint in §4. Concluding remarks are presented in §5.

## 2. Formulation and calculation method

In this study, we consider a stably stratified fluid motion governed by the Navier-Stokes equation with the Boussinesq approximation, specifically written as

$$\frac{\partial \mathbf{u}}{\partial t} + \mathbf{u} \cdot \nabla \mathbf{u} = -\nabla p + Nb \mathbf{e}_v + \nu \nabla^2 \mathbf{u} \quad (2.1a)$$

$$\frac{\partial b}{\partial t} + \mathbf{u} \cdot \nabla b = -N \mathbf{u} \cdot \mathbf{e}_v + \kappa \nabla^2 b, \quad (2.1b)$$

where  $\mathbf{u}$  is the three-dimensional velocity vector satisfying the incompressible condition,  $\nabla \cdot \mathbf{u} = 0$ ,  $p$  is the pressure divided by the reference density,  $b$  is the buoyancy,  $N$  is the buoyancy frequency supposed to be constant,  $\nu$  is the kinematic viscosity,  $\kappa$  is the diffusivity, and  $\mathbf{e}_v$  is the unit vector pointing upwards. Here,  $b$  is scaled so as to have the unit of velocity and related to the fluid density,  $\rho$ , as  $\rho = \rho_{ref}(1 - N^2 X_3/g - Nb/g)$ , where  $g$  is the acceleration of gravity,  $\rho_{ref}$  is the reference density, and  $X_3$  is the vertical coordinate.

We envisage a plane internal gravity wave propagating in a direction with an angle  $\theta$  against the vertical direction. Let us assign the  $x_3$ -axis to this direction, the  $x_1$ -axis to the direction of the flow velocity, and the  $x_2$ -axis perpendicular to them (figure 1a). In the following, velocity components along the  $x_1$ -,  $x_2$ -, and  $x_3$ -axes are respectively represented as  $u_1$ ,  $u_2$ , and  $u_3$ . We may write the ordinary coordinates  $(X_1, X_2, X_3)$ , with  $X_3$  pointing to  $\mathbf{e}_v$ , as  $X_1 = x_1 \cos \theta + x_3 \sin \theta$ ,  $X_2 = x_2$ ,  $X_3 = -x_1 \sin \theta + x_3 \cos \theta$ . Then, we cut out a small domain from this wave field (figure 1b). By assuming that the wavelength is asymptotically larger than the domain size, we may reduce a solution of (2.1) into the following form:  $(u_1, u_2, u_3, b, p) = (Sx_3, 0, 0, Mx_3, Qx_3^2/2)$ , i.e., velocity and buoyancy linearly vary along  $x_3$ . Inserting this expression into (2.1) allows us to find the coefficients, which are the spatial gradients in the variables, as

$$S(t) = S_0 \cos(\omega t + \alpha) \quad (2.2a)$$

$$M(t) = S_0 \sin(\omega t + \alpha) \quad (2.2b)$$

$$Q(t) = NS_0 \cos \theta \sin(\omega t + \alpha) \quad (2.2c)$$

$$\omega = N \sin \theta. \quad (2.2d)$$

Here,  $S_0$  represents the maximum velocity shear and  $\alpha$  is the initial phase of the background wave that is arbitrarily chosen. The wave frequency  $\omega$  is linked to the propagation angle  $\theta$  via the dispersion relation of internal gravity waves (2.2d).

Next, we consider disturbances superimposed on this wave solution. Variables are rewritten as  $(u_1, u_2, u_3, b, p) = (Sx_3 + u'_1, u'_2, u'_3, Mx_3 + b', Qx_3^2/2 + p')$ . A new coordinate system that moves following the background velocity is introduced as  $\xi_1 = x_1 - \int Sx_3 dt$ ,  $\xi_2 = x_2$ ,  $\xi_3 = x_3$  (see, again, figure 1b). The governing equations for the disturbance components are now

$$\frac{\partial u'_i}{\partial t} + \frac{\partial u'_j u'_i}{\partial \xi_j} + S \delta_{i1} u'_3 = -\frac{\partial p'}{\partial \xi_i} + Nb'(\cos \theta \delta_{i3} - \sin \theta \delta_{i1}) + \nu \frac{\partial^2 u'_i}{\partial \xi_j^2} \quad (2.3a)$$

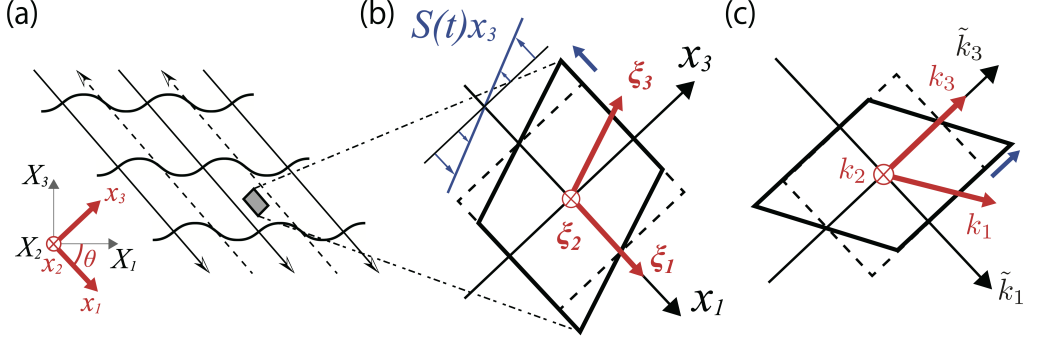


FIGURE 1. (a) We consider an internal gravity wave obliquely propagating in a stratified fluid. Thick black curves represent the isopycnal surfaces and the arrows indicate the direction of the flow velocity. A cartesian coordinate system,  $(x_1, x_2, x_3)$ , is arranged such that  $x_1$  points to the direction of the flow velocity,  $x_3$  to the velocity gradient, and  $x_2$  perpendicular to them. (b) We cut out a small domain from the internal wave field, in which the velocity shear  $S$  is regarded as spatially constant but depends on time. A time-dependent coordinate system,  $(\xi_1, \xi_2, \xi_3)$ , that follows the background flow velocity is introduced. The shape of the model domain (thick parallelogram) is fixed in the  $\xi$  frame and hence distorted periodically with time. (c) The wavenumber coordinates,  $(k_1, k_2, k_3)$ , which are defined by taking Fourier transform with respect to  $(\xi_1, \xi_2, \xi_3)$ , also vary with time.

$$\frac{\partial b'}{\partial t} + \frac{\partial u'_j b'}{\partial \xi_j} + M u'_3 = -N(\cos \theta u'_3 - \sin \theta u'_1) + \kappa \frac{\partial^2 b'}{\partial \xi_j^2} \quad (2.3b)$$

$$\frac{\partial u'_j}{\partial \xi_j} = 0, \quad (2.3c)$$

where  $\partial/\partial \xi_i \equiv \partial/\partial \xi_i - \int S dt \delta_{i3} \partial/\partial \xi_1$ ,  $i$  and  $j$  represent 1, 2 or 3, and the summation convention for repeated indices are used.

It is noteworthy that, when we neglect the nonlinear, viscosity, and diffusion terms, the system of equations (2.3) reduces to the model proposed by Ghaemsaïdi & Mathur (2019). As shown by their stability analysis, of this model, several kinds of instability occur depending on the angle and the amplitude of the outer wave. Thus, the energy of the system is spontaneously amplified even without any external forcing term. Here, we shall call this process “local instability” of internal waves.

In the present system, budgets of the kinetic energy and the available potential energy are governed by

$$\frac{d}{dt} \underbrace{\left\langle \frac{u_i'^2}{2} \right\rangle}_{\mathcal{E}_K} = \underbrace{-S \langle u'_1 u'_3 \rangle}_{\mathcal{P}_K} + \underbrace{N \cos \theta \langle u'_3 b' \rangle - N \sin \theta \langle u'_1 b' \rangle}_{\mathcal{C}} - \underbrace{\nu \left\langle \left( \frac{\partial u'_i}{\partial \xi_j} \right)^2 \right\rangle}_{\epsilon} \quad (2.4a)$$

$$\frac{d}{dt} \underbrace{\left\langle \frac{b'^2}{2} \right\rangle}_{\mathcal{E}_P} = \underbrace{-M \langle u'_3 b' \rangle}_{\mathcal{P}_P} + \underbrace{-N \cos \theta \langle u'_3 b' \rangle + N \sin \theta \langle u'_1 b' \rangle}_{-\mathcal{C}} - \underbrace{\kappa \left\langle \left( \frac{\partial b'}{\partial \xi_j} \right)^2 \right\rangle}_{\epsilon_P}, \quad (2.4b)$$

where  $\langle \rangle$  denotes the spatial averaging over the whole domain. From these expressions, we understand that the kinetic energy,  $\mathcal{E}_K$ , and the available potential energy,  $\mathcal{E}_P$ , are produced by the terms  $\mathcal{P}_K$  and  $\mathcal{P}_P$ , respectively, exchanged through the term  $\mathcal{C}$ , and eventually dissipated in heat and background potential energies, at the rate of  $\epsilon$  and  $\epsilon_P$ , respectively. At variance with the vertically sheared horizontal flow cases, the sign of the

$\mathcal{E}_K$ - $\mathcal{E}_P$  conversion rate  $\mathcal{C}$  is not determined a priori; it depends on the relative magnitudes of production and dissipation terms.

In this study, equations (2.3) are numerically solved in the wavenumber domain  $\mathbf{k}$  using the Fourier spectral method by assuming triply periodic boundary conditions with respect to  $\xi_j$  (not to  $X_j$  or  $x_j$ ). Since the physical coordinates  $\xi_j$  now explicitly depend on time, the wavenumber coordinates also vary with time; specifically, when we write the wavenumber in the fixed frame as  $\tilde{\mathbf{k}} = (\tilde{k}_1, \tilde{k}_2, \tilde{k}_3)$ , the wavenumber for the moving frame  $\mathbf{k} = (k_1, k_2, k_3)$  follows  $k_1 = \tilde{k}_1, k_2 = \tilde{k}_2, k_3 = \tilde{k}_3 + \int S dt \tilde{k}_1$  (figure 1c). For the calculation, we basically follow the procedure by Chung & Matheou (2012); the viscous and diffusive terms are analytically solved by the integration factor method, the pressure terms are diagnosed at each step enforcing the incompressibility constraint. The remaining terms are integrated using the low-storage third-order Runge-Kutta scheme of Spalart *et al.* (1991). The aliasing errors are eliminated by the combination of wavenumber truncation and phase shifting. Different from the stationary shear cases, we do not remesh the grid during the calculation because the effect from grid skewing would be minor compared to the aliasing error arising from remeshing in the present settings. The calculation domain is a cubic box and the grid spacing is equivalent in all directions. To ensure the stability of calculation, as well as to sufficiently resolve buoyancy oscillation, the time step  $\Delta t$  is controlled via a modified form of the Courant-Friedrichs-Lewy condition such that  $\Delta t \leq \min(1.83/\max(\mathbf{u} \cdot \mathbf{k}), 0.1/N)$ .

The non-dimensional control parameters in the experiments are the external Froude number,  $Fr = S_0/N$ , the external Reynolds number,  $Re = S_0 L^2/\nu$ , the Prandtl number,  $Pr = \nu/\kappa$ , and the wave frequency divided by the buoyancy frequency,  $\omega/N$ . Here, we have introduced the domain length  $L$ , which is fixed to be  $2\pi$  in our model. For thermally stratified ocean, the Prandtl number is around 7 but for simplicity it is set to unity here. The Reynolds number and the Froude number are now defined based on the external conditions and should be distinguished from those determined by the length and velocity scales of turbulence. In this study, we fix  $Re$  to be 300000 but vary  $Fr$  from 0.1 to 1.2. The wave frequency is set relatively high,  $\omega/N = 0.6$ , to avoid excessive distortion of the domain shape. According to Ghaemsaïdi & Mathur (2019), although the density overturn or the shear instability does not occur in this parameter regime, disturbances are expected to be amplified through parametric subharmonic instability (PSI).

The initial condition is an isotropic Gaussian white noise added both for the velocity and buoyancy fields. As will be shown in §3, the energy of the system first decreases because of viscosity and diffusivity before being enhanced later, to reach a saturation level. To reduce the computation cost, the total number of grid points is first set as  $512^3$  with the spherical truncation of wavenumbers at the 241 mode, and later raised up to  $1024^3$  with the truncation at the 482 mode before the turbulence energy is fully developed. It is noted that, although a quasi-stationary state is expected to be reached in each run, the high computational cost inhibits us from conducting experiments over a so long period. In this study, the total calculation time is varied depending on  $Fr$ , as listed in table 1, since an experiment with smaller  $Fr$  tends to require a longer time to reach a state of energy saturation. To quantify statistical properties of turbulence, we averaged data over one wave period,  $t_{\text{end}} - T < t \leq t_{\text{end}}$ , where  $t_{\text{end}}$  is the total calculation time and  $T \equiv 2\pi/\omega$  is the period of the outer wave. To ensure the sufficiency of model resolution, we checked the Kolmogorov scale  $\eta_K = (\nu^3/\epsilon)^{1/4}$  and the Ozmidov scale  $\eta_O = (\epsilon/N^3)^{1/2}$ , which are the lower and upper bounds of the range of isotropic turbulence. Then, we confirmed that both are resolved in all experiments. For example, we show in table 1 the values of  $\eta_K k_{\text{max}}$ , the Kolmogorov scale multiplied by the maximum wavenumber, which should be larger than 1 according to de Bruyn Kops & Riley (1998).

---

$Fr$	$t_{\text{end}}$	$Re_b$	$Fr_t$	$\epsilon_P/(\epsilon + \epsilon_P)$	$\mathcal{P}_P/(\mathcal{P}_K + \mathcal{P}_P)$	$\eta_K k_{max}$
0.1	85T	1.55	0.014	0.41	0.54	1.6
0.2	40T	4.74	0.036	0.38	0.55	1.7
0.3	32T	62.6	0.066	0.35	0.53	1.1
0.4	25T	32.5	0.078	0.34	0.61	1.5
0.5	19T	86.9	0.099	0.36	0.56	1.3
0.6	16T	47.8	0.105	0.37	0.62	1.6
0.7	13T	43.1	0.057	0.37	0.78	1.8
0.8	12T	188	0.088	0.40	0.95	1.3
0.9	11T	475	0.178	0.45	0.70	1.1
1.0	9T	611	0.212	0.44	0.67	1.1
1.1	8T	373	0.090	0.47	1.08	1.3
1.2	7T	571	0.173	0.47	0.61	1.2

---

TABLE 1. Values of the control parameter  $Fr \equiv S_0/N$ , the total calculation time  $t_{\text{end}}$ , and the dimensionless quantities obtained in each run. Here,  $Re_b \equiv \epsilon/(\nu N^2)$  is the buoyancy Reynolds number,  $Fr_t \equiv \epsilon/(N\mathcal{E}_K)$  is the turbulent Froude number, and  $\eta_K \equiv (\nu^3/\epsilon)^{1/4}$  is the Kolmogorov scale. To obtain  $\epsilon$ ,  $\epsilon_P$ ,  $\mathcal{E}_K$ ,  $\mathcal{P}_K$ , and  $\mathcal{P}_P$ , temporal averages are taken over  $t_{\text{end}} - T < t \leq t_{\text{end}}$ .

---

### 3. Results

We demonstrate the simulation results of a specific case,  $Fr = 0.4$ , to reveal the basic mechanisms of turbulence enhancement in the model. The time evolutions of  $\mathcal{E}_K$ ,  $\mathcal{E}_P$ , and their sum are shown in figure 2a. After a rapid decay within a couple of wave periods of both the kinetic and available potential energies due to viscosity and diffusivity, they are exponentially enhanced while periodically exchanging energy. The step-like behavior of the total energy results from the oscillation in its production rates,  $\mathcal{P}_K + \mathcal{P}_P$ . At around  $t \sim 18T$ , the enhancement is retarded and will gradually reach a saturation level.

Figure 2b-d show snapshots of the buoyancy perturbation  $b'$  on the surface of the calculation domain at  $t = 15T, 18T$ , and  $25T$ . Note that different color scales are used for each panel. A notable feature is the striped pattern appearing during the stage of exponential energy growth (figure 2b). To discuss the mechanism of energy enhancement, we show in figure 2e-f the energy spectra in the horizontal and vertical section at each stage. According to the dispersion relation of internal gravity waves, the angle of the wave vector against the vertical axis  $\phi$  determines the wave frequency as  $\sigma = N \sin \phi$ . In figure 2e, we find energy concentration along the line  $N \sin \phi = \omega/2$ . This result indicates that the subharmonic component of the outer wave is selectively enhanced and, consequently, the striped pattern that is perpendicular to these wave vectors is made visible. Going back to figure 2a, one may notice the exchange of  $\mathcal{E}_K$  and  $\mathcal{E}_P$  occurring with the same frequency as that of the outer wave, which indicates the oscillatory motion of disturbances with half the frequency of the outer wave. All of these features suggest that disturbance waves are enhanced by PSI.

When the amplitude of the disturbance waves reaches the overturning threshold, around  $t \sim 18T$ , secondary instabilities arise and produce much smaller-scale fluctuations (figure 2c). At this stage, the energy accumulated in the low-wavenumber region is abruptly transferred to high-wavenumber components (figure 2f). After a sufficiently long time (figure 2d, g), a smooth and nearly isotropic energy spectrum is formed, except for the lowest-wavenumber region, where anisotropic structures are maintained such that the PSI continues to supply energy into the system. For a better visualisation, please also see the supplementary movie that shows buoyancy perturbation on the domain surface across the phases of the onset of PSI, secondary instability, and the fully developed turbulence.

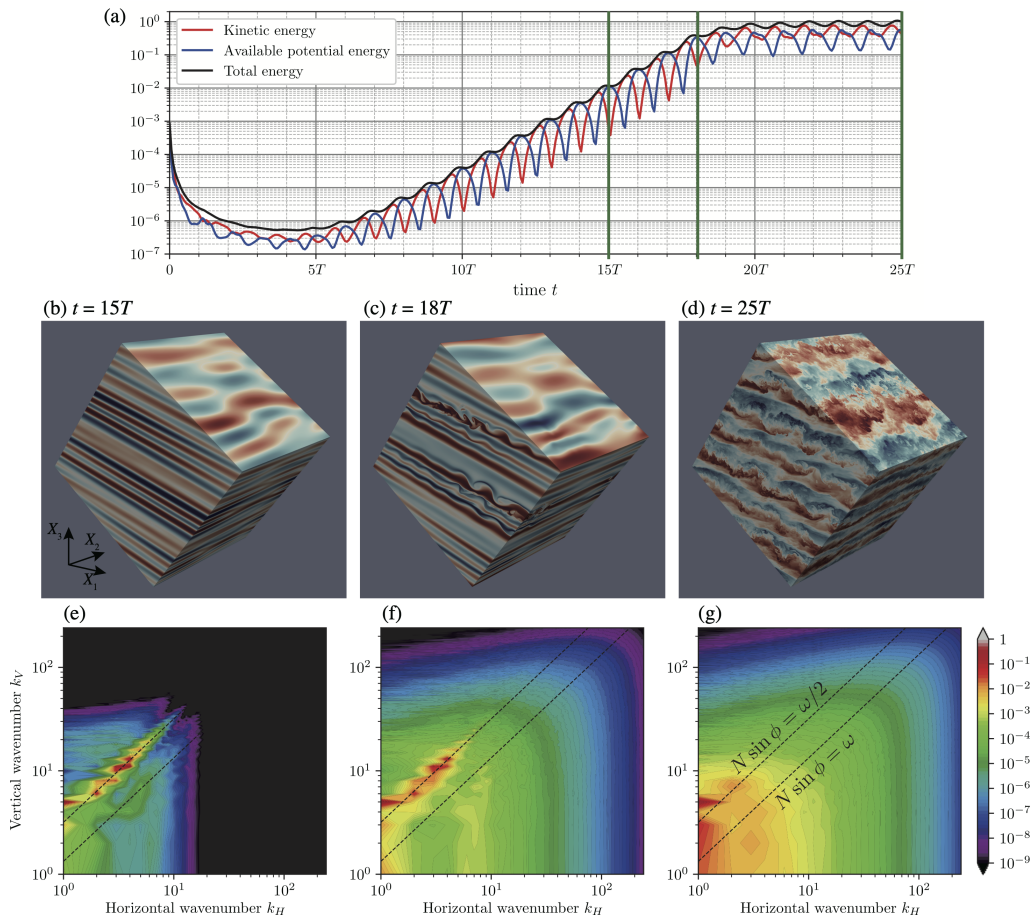


FIGURE 2. Results of the experiment with  $Fr = 0.4$ . (a) Time series of the kinetic energy (red), the available potential energy (blue), and their sum (black). They are normalised such that the total energy becomes 1 at the end of the experiment. The vertical green lines indicate  $t = 15T, 18T$ , and  $25T$ , the times that the following panels correspond to. (b)-(d) Buoyancy perturbation  $b'$  on the surface of the calculation domain at  $t = 15T$ (b),  $18T$ (c), and  $25T$ (d). Red and blue correspond to positive and negative values. Different color scales are used for three panels. (e)-(g) Energy spectra in the horizontal and vertical wavenumber space,  $E(k_H, k_V)$ , at  $t = 15T$ (e),  $18T$ (f), and  $25T$ (g). The spectra are integrated over the azimuthal angle and normalised such that  $\int E(k_H, k_V) dk_H dk_V = 1$ . The black dotted lines indicate  $N \sin \phi = \omega$  and  $N \sin \phi = \omega/2$ , where  $\phi$  is the angle of the wavevector against the vertical axis.

Even in other experiments with various  $Fr$ , the process is essentially the same; first, specific low-wavenumber components are selectively amplified and, next, secondary instability redistributes energy across spectral space to the smallest scales.

#### 4. Discussion

The relative importance between the production rates of available potential energy and kinetic energy is quantified by evaluating  $\mathcal{P}_P/(\mathcal{P}_K + \mathcal{P}_P)$ . As shown in table 1, this ratio is always larger than 0.5. Thus, we derive  $\mathcal{P}_P > \mathcal{P}_K$ ; i.e., the instability mainly causes the production of available potential energy. We next analyse the fraction of dissipation rates of available potential energy in the total energy loss, or the so-called mixing efficiency,

$\epsilon_P/(\epsilon+\epsilon_P)$ . This value is, on the other hand, always less than 0.5 so that  $\epsilon > \epsilon_P$  holds; i.e., the kinetic energy dissipation rate is larger than the available potential energy dissipation rate. These contrasting results indicate that part of available potential energy injected from the outer wave is converted into the kinetic energy and dissipated in heat. Figure 3a shows the mixing coefficient  $\Gamma = \epsilon_P/\epsilon$  as a function of  $Fr = S_0/N$ . Compared to  $\Gamma = 0.2$  that has been traditionally assumed for the ocean (Gregg *et al.* 2018), the present results that always hold  $\Gamma > 0.5$  are substantially larger. Except for  $Fr \leq 0.2$  cases,  $\Gamma$  tends to increase in accordance with  $Fr$  and becomes close to 1 in  $Fr > 1.0$  cases. It should be kept in mind that, when  $Fr$  is small, effects from viscosity and diffusivity become relatively large, possibly leading to the property of small-scale turbulence being much different from the large  $Fr$  cases. In general, effect from viscosity to stratified turbulence can be judged from buoyancy Reynolds number,  $Re_b = \epsilon/(\nu N^2)$ , which is equivalent to the ratio between  $\eta_O$  and  $\eta_K$ . As shown in table 1, in the cases of  $Fr = 0.1$  and  $0.2$ ,  $Re_b$  is of the order of unity, so that the inertial subrange where isotropic turbulence exists collapses. This peculiarity might cause the exceptional behavior of  $\Gamma$  for these cases.

Recently, based on the scaling arguments and the DNS data analysis, Maffioli *et al.* (2016) and Garanaik & Venayagamoorthy (2019) suggested that the turbulent Froude number, defined as  $Fr_t \equiv \epsilon/(NU^2)$ , where  $U$  is the typical velocity of turbulence, would be a good indicator of the mixing coefficient. According to them,  $\Gamma$  becomes maximum of around 0.5 at  $Fr_t \sim 0.3$  and converges to around 0.33 for  $Fr_t \rightarrow 0$ . In this study, by regarding  $\mathcal{E}_K$  as  $U^2$ , we estimate the turbulent Froude number in each run. As figure 3b shows, although it is true that  $\Gamma$  seems to weakly depend on  $Fr_t$ , they do not follow the functional relationship suggested in previous studies. More classically,  $Re_b$  that involves the effect from viscosity is known to be a candidate for the indicator of  $\Gamma$  (Gregg *et al.* 2018). Figure 3a also exhibits a tendency for  $\Gamma$  to increase with  $Re_b$ . However, since  $Re_b$  is inevitably correlated with  $Fr$  in the current settings, causality is still uncertain.

A difference in the situations between previous studies and ours is the source of turbulence energy. In Garanaik & Venayagamoorthy (2019), they used three kinds of data sets of DNS experiments: freely decaying turbulence, forced turbulence, and sheared stratified turbulence. In every case, energy is initially injected to kinetic energy and only in a second stage part of it is converted to available potential energy to mix the stratification. In the present case, on the other hand, kinetic energy and available potential energy are simultaneously enhanced by PSI and the latter is directly used for mixing. From the viewpoint of energetics, this process is intermediate between the conventional shear instability that is caused by the conversion from mean to turbulent kinetic energy and the convection caused by release of available potential energy. Taking into account the fact that in free convection the mixing coefficient occasionally exceeds 1.0 (Davies Wykes & Dalziel 2014), we can conclude that the result in our experiments,  $0.5 < \Gamma < 1.0$ , which connects the regimes of vertical shear-induced mixing and convectively driven mixing, is reasonable.

## 5. Concluding remarks

In this study, we have developed a new technique for direct numerical simulation (DNS) of stratified turbulence generated by instability of internal gravity waves. A novelty of our method is to distort the model domain obliquely and periodically to simulate a turbulence enhancement due to unresolved large-scale internal waves while fully resolving the smallest-scale energy dissipation range. We use the term “local instability” to represent the exponential amplification of disturbance energy in an infinitely-large scale internal wave. Attention is paid to the small-Froude number regime where the



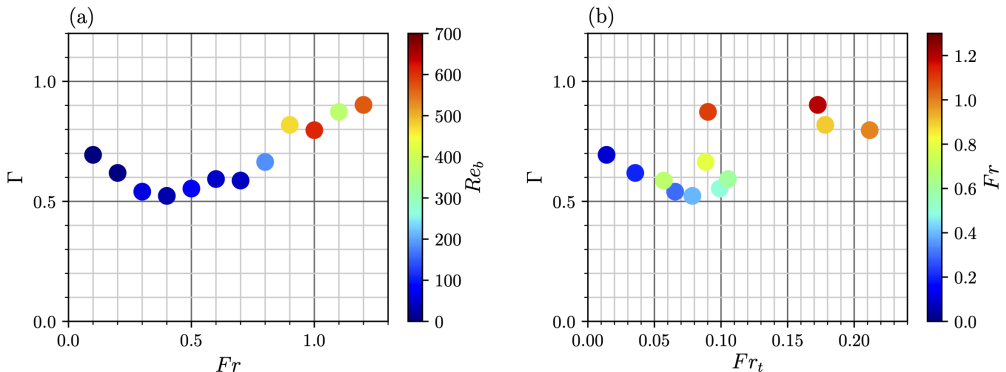


FIGURE 3. (a) Mixing coefficient  $\Gamma \equiv \epsilon_P/\epsilon$  as a function of (external) Froude number  $Fr \equiv S_0/N$ . The color represents the turbulent Froude number  $Fr_t \equiv \epsilon/(N\mathcal{E}_K)$ . (b) Mixing coefficient  $\Gamma$  as a function of turbulent Froude number  $Fr_t$ . The color represents the buoyancy Reynolds number  $Re_b \equiv \epsilon/(\nu N^2)$ . Here, the energy dissipation rates  $\epsilon$  and  $\epsilon_P$  and the kinetic energy density  $\mathcal{E}_K$  are obtained by averaging each over  $t_{\text{end}} - T < t \leq t_{\text{end}}$ .

parametric subharmonic instability (PSI) excites a striped pattern of disturbance waves. We found that, when the amplitude of the disturbance waves reaches the overturning threshold, secondary instabilities abruptly occur to transfer energy to much smaller-scale fluctuations, resulting in an efficient mixing.

The scaling relationship between the turbulent Froude number  $Fr_t$  and the mixing coefficient  $\Gamma$  recently proposed by Garanaik & Venayagamoorthy (2019) is, at least in the range of  $Fr_t \lesssim 0.2$ , not supported in our numerical experiments. This discrepancy might be related to the difference in energy source. We suppose that when the available potential energy of turbulence is directly supplied from large-scale fluid motion rather than converted from turbulent kinetic energy, it is more efficiently used for vertical mixing. This thought agrees with Ijichi *et al.* (2020), who found values as large as  $\Gamma = 0.8$  near the sea floor in the Brazil Basin where hydraulic overflows are thought to cause convection, and also with the latest DNS study by Howland *et al.* (2020).

Although our model does not involve the effect of rotation at the current stage, it should be an important factor. According to the linear theory of inertia-gravity wave, rotation changes the partitioning of kinetic and available potential energies. Specifically, if the rotation axis is parallel to the gravity direction, the following relationship holds; (kinetic energy)/(available potential energy) =  $(1 - \omega^2/N^2)(\omega^2 + f^2)/(\omega^2 - f^2)$ , where  $\omega$  is the wave frequency and  $f$  is the Coriolis parameter (Polzin & Lvov 2011). Consequently, as for near-inertial waves,  $\omega \sim f$ , a large part of the energy is contained in the kinetic part so that the mixing efficiency is expected to be lowered. In the real ocean, it has been reported that PSI plays a special role in transferring energy of tide-generated internal waves into near-inertial waves (Hibiya & Nagasawa 2004). Therefore, in order to get a better insight into the wave-driven ocean mixing, it is vital in future research to examine how the rotation affects the energy budgets of both the internal waves and turbulence.

## Acknowledgements

This research was supported by JSPS KAKENHI Grant JP18H04918 and JP20K14556. Numerical calculation was conducted using the Fujitsu PRIMERGY CX600M1/CX1640M1 (Oakforest-PACS) at the Information Technology Center of the University of Tokyo.

## Declaration of interests

The authors report no conflict of interest.

## REFERENCES

- DE BRUYN KOPS, S. M. & RILEY, J. J. 1998 Direct numerical simulation of laboratory experiments in isotropic turbulence. *Physics of Fluids* **10** (9), 2125–2127.
- CHUNG, D. & MATHEOU, G. 2012 Direct numerical simulation of stationary homogeneous stratified sheared turbulence. *Journal of Fluid Mechanics* **696**, 434–467.
- DAUXOIS, T., PEACOCK, T., BAUER, P., CAULFIELD, C. P., CENEDESE, C., GORL, C., HALLER, G., IVEY, G. N., LINDEN, P. F., MEIBURG, E., PINARDI, N. & WOODS, A. 2020 Confronting grand challenges in environmental fluid dynamics. *submitted*.
- DAVIES WYKES, M.S. & DALZIEL, S.B. 2014 Efficient mixing in stratified flows: experimental study of a RayleighTaylor unstable interface within an otherwise stable stratification. *Journal of Fluid Mechanics* **756**, 1027–1057.
- FRITTS, D. C., WANG, L., WERNE, J., LUND, T. & WAN, K. 2009 Gravity wave instability dynamics at high Reynolds numbers. Part I: Wave field evolution at large amplitudes and high frequencies. *Journal of the Atmospheric Sciences* **66** (5), 1126–1148.
- GARANAİK, A. & VENAYAGAMOORTHY, S. K. 2019 On the inference of the state of turbulence and mixing efficiency in stably stratified flows. *Journal of Fluid Mechanics* **867**, 323–333.
- GHAEMSAIDI, S. J. & MATHUR, M. 2019 Three-dimensional small-scale instabilities of plane internal gravity waves. *Journal of Fluid Mechanics* **863**, 702–729.
- GREGG, M. C., D’ASARO, E. A., RILEY, J. J. & KUNZE, E. 2018 Mixing efficiency in the ocean. *Annual Review of Marine Science* **10** (1), 443–473.
- HIBIYA, T. & NAGASAWA, M. 2004 Latitudinal dependence of diapycnal diffusivity in the thermocline estimated using a finescale parameterization. *Geophysical Research Letters* **31** (1).
- HOWLAND, C. J., TAYLOR, J. R. & CAULFIELD, C. P. 2020 Mixing in forced stratified turbulence and its dependence on large-scale forcing. *Journal of Fluid Mechanics* **898**, A7.
- IJICHI, T., ST. LAURENT, L., POLZIN, K. L. & TOOLE, J. M. 2020 How variable is mixing efficiency in the abyss? *Geophysical Research Letters* **47** (7), e2019GL086813.
- MACKINNON, J. A., ZHAO, Z. & OTHERS 2017 Climate process team on internal wavedriven ocean mixing. *Bulletin of the American Meteorological Society* **98** (11), 2429–2454.
- MAFFIOLI, A., BRETHOUWER, G. & LINDBORG, E. 2016 Mixing efficiency in stratified turbulence. *Journal of Fluid Mechanics* **794**, R3.
- MUNK, W. & WUNSCH, C. 1998 Abyssal recipes II: energetics of tidal and wind mixing. *Deep Sea Research Part I* **45** (12), 1977–2010.
- OSBORN, T. R. 1980 Estimates of the local rate of vertical diffusion from dissipation measurements. *Journal of Physical Oceanography* **10** (1), 83–89.
- POLZIN, K. L. & LVOV, Y. V. 2011 Toward regional characterizations of the oceanic internal wavefield. *Reviews of Geophysics* **49** (4).
- PORTWOOD, G. 2019 A study on homogeneous sheared stably stratified turbulence. PhD Thesis, University of Massachusetts Amherst.
- ROGALLO, R. S. 1981 Numerical experiments in homogeneous turbulence. *NASA Tech. Rep.* (81315).
- SALEHIPOUR, H., CAULFIELD, C. P. & PELTIER, W. R. 2016 Turbulent mixing due to the Holmboe wave instability at high Reynolds number. *Journal of Fluid Mechanics* **803**, 591–621.
- SMYTH, W. D., MOUM, J. N. & CALDWELL, D. R. 2001 The efficiency of mixing in turbulent patches: Inferences from direct simulations and microstructure observations. *Journal of Physical Oceanography* **31** (8), 1969–1992.
- SPALART, P. R., MOSER, R. D. & ROGERS, M. M. 1991 Spectral methods for the Navier-Stokes equations with one infinite and two periodic directions. *Journal of Computational Physics* **96** (2), 297–324.
- THORPE, S. A. 2005 *The Turbulent Ocean*. Cambridge University Press.